Journal of The
Electrochemical Society

OPEN ACCESS

Silicon-Based Nanocomposite Anodes with Excellent Cycle Life for Lithium-Ion Batteries Achieved by the Synergistic Effect of Two Silicides

To cite this article: Yasuhiro Domi *et al* 2024 *J. Electrochem. Soc.* **171** 080506

Journal of The Electrochemical Society, 2024 **171** 080506

Silicon-Based Nanocomposite Anodes with Excellent Cycle Life for Lithium-Ion Batteries Achieved by the Synergistic Effect of Two Silicides

Yasuhiro Domi,[1,2,z] Hiroyuki Usui,[1,2] Takumi Okasaka,[1,3] Kei Nishikawa,[4] and Hiroki Sakaguchi[1,2,z]

[1]*Department of Chemistry and Biotechnology, Graduate School of Engineering, Tottori University, Minami 4-101, Koyama-cho, Tottori 680-8552, Japan*
[2]*Center for Research on Green Sustainable Chemistry, Tottori University, Koyama-cho, Tottori 680-8552, Japan*
[3]*Department of Engineering, Graduate School of Sustainability Science, Tottori University, Koyama-cho, Tottori 680-8552, Japan*
[4]*Center for Green Research on Energy and Environmental Materials, National Institute for Materials Science (NIMS), Tsukuba 305-0044, Japan*

Nanocomposite electrodes comprising $LaSi_2$ and Si exhibit satisfactory charge–discharge cycling performances but their capacity is degraded after repeated cycles. A metallographic structure, in which the Si phase was finely dispersed in the $LaSi_2$ matrix phase, was formed before cycling. The elastic $LaSi_2$ relieved Si-generated stress and suppressed electrode disintegration. Contrarily, the $LaSi_2$ phase in the metallographic structure was surrounded by the Si matrix phase after cycling. The positional relationship between the two phases was reversed, and $LaSi_2$ could not relieve the stress. For a nanocomposite electrode containing $CrSi_2$, which exhibits stiffness to withstand the Si-generated stress, the structural changes were suppressed after cycling, resulting in good cycling stability. Here, we considered that the addition of stiff silicides as a third phase to the $LaSi_2$/Si composite could improve the cycle life. Thus, this study prepared nanocomposite electrodes containing elastic $LaSi_2$, stiff MSi_2 (where M = Cr, Mo, Nb, Ta, Ti, or W), and elemental Si and investigated their electrochemical performances. Reaction behaviors, such as the metallographic structure, electrode thickness, and phase transition, were also clarified. The $LaSi_2$/$NbSi_2$/Si electrode exhibited the best cycle life without changes in its metallographic structure owing to the synergistic effect of stiff and elastic silicides.
 [DOI: 10.1149/1945-7111/ad69c6]

Manuscript submitted April 2, 2024; revised manuscript received July 5, 2024. Published August 7, 2024.

Supplementary material for this article is available online

High-performance rechargeable batteries are essential for the establishment of a decarbonized society.[1–4] Owing to their high energy densities, lithium-ion batteries (LIBs) are widely used as power sources in mobile electronic devices and electric vehicles (EVs). As a power source for EVs, the performance of LIBs, in terms of high energy density, long life, safety, and fast charge–-discharge, requires improvement. Si is preferred as a next-generation active material for LIB anodes because its theoretical capacity is approximately 10 times that of the currently used graphite electrode (crystalline $Li_{3.75}Si$: 3580 mA h g^{-1}; LiC_6: 372 mA h g^{-1}).[5–8] Thus, Si-based anodes are highly desirable; however, the large volume change associated with Si lithiation (charging) and delithiation (discharging) hinders its practical application. The volume expansion ratio of Si to the crystalline $Li_{3.75}Si$ phase can be as high as 280%, resulting in high stress and strain in active materials.[5,9] We previously reported that the expansion ratio considerably exceeded 280% owing to the formation of voids and cracks in the active material during charge–discharge tests.[10] Furthermore, Si exhibits high electrical resistivity, low initial Coulombic efficiency (CE), and a low Li^+ diffusion coefficient, which limit its application.[11–13]

Several approaches have been employed to address the aforementioned limitations. They include the synthesis of nanostructured Si materials (i.e., nanoparticles, nanowires, and nanorods) to relieve Si-generated stress,[14–19] Si coating using conductive materials to reduce the electrical resistivity of Si,[20,21] doping of Si with impurities (e.g., phosphorus and boron) to improve its electrical conductivity and alter its phase transition behavior,[22–27] and prelithiation of Si to enhance the initial CE.[28–30] Furthermore, we proposed futuristic Si-based active materials, e.g., binary silicide/Si composites, to address the limitations of Si.[31–34] In particular, the $LaSi_2$/Si electrode exhibited the best cyclability among several binary silicide/Si composites. In addition, the electrochemical performance of the ternary silicide/Si composite electrode was superior to that of the binary silicide/Si electrode.[35–38] We established that composite materials should possess mechanical properties to accommodate Si-induced stress, low electrical resistivity, adequate reactivity with Li^+, and high thermodynamic stability that does not deteriorate even after repeated charge–discharge cycling.[13,31,32,34]

It is essential to understand the degradation mechanism of the $LaSi_2$/Si electrode and mitigate it to improve electrochemical performance. Prior to charge–discharge cycling, a metallographic structure was formed, in which Si phases with a diameter of several hundred nanometers were finely dispersed in $LaSi_2$ matrix phases.[39] This metallographic structure resulted in good cycling stability because the elastic properties of $LaSi_2$ mitigated the Si-generated stresses and suppressed electrode disintegration. Contrarily, prior to the capacity degradation, the microstructure changed into a structure in which the $LaSi_2$ phase was finely dispersed in the Si matrix phase, i.e., the positional relationship between the two phases was reversed. The elastic $LaSi_2$ matrix ruptured and reduced in size, owing to the Si-generated stress. Thus, it was concluded that the $LaSi_2$ phase could no longer relieve the Si-generated stress and that the $LaSi_2$/Si electrode deteriorated as a result.

Composites containing $CrSi_2$, instead of elastic silicide exhibit a metallographic structure, in which the Si phase surrounds the silicide phase, preventing microstructural changes even after charge–-discharge cycles (Figs. S1 and S2).[37,40] $CrSi_2$/Si exhibits stiffness to resist the Si-generated stress. Consequently, the $CrSi_2$/Si electrode exhibited good cycle stability. This implies that the addition of $CrSi_2$ as a third phase to a $LaSi_2$/Si electrode can improve the cycle life because microstructure inversion can be suppressed and $LaSi_2$ can relieve the Si-generated stress. In addition, Si is known to soften due to lithiation, and the introduction of the $CrSi_2$ as a support framework is essential to suppress electrode disintegration due to the

[z]E-mail: domi@tottori-u.ac.jp; sakaguch@tottori-u.ac.jp

softening. This study prepared nanocomposite electrodes comprising elastic $LaSi_2$, stiff $CrSi_2$, and elemental Si and investigated their electrochemical performance. Reaction behaviors such as the metallographic structure, electrode thickness, and amount of Li-rich phase ($x = 2.00$–3.75 in Li_xSi) formed, were clarified. The effect of stiffness on the electrochemical performance was also investigated. Although the effects of the Si grain size on the microstructural stability and electrochemical performance of Si-based composite electrodes have been reported,[41] the differences in the mechanical functions of Si alloys have not been examined, as far as we know. This study closes that knowledge gap by clarifying the effects of various silicide functions on the charge–discharge characteristics of Si-based electrodes.

Experimental Methods

Synthesis of $LaSi_2$/MSi_2/Si composites.—A Si-based nanocomposite comprising two functional silicides and elemental Si was synthesized through a mechanical alloying (MA) method. We considered $LaSi_2$ and $CrSi_2$ to be elastic and stiff silicides, respectively. A thin La shot (Santoku Corp.) was fabricated using a press machine, and fine chips were obtained using a nipper. We placed a mixture of elemental La chips, Cr powder (Nilaco Corp.), and Si powder (FUJIFILM Wako Pure Chemical Corporation, Ltd.; preparation weight ratio of 35/35/30 for the $LaSi_2$/$CrSi_2$/Si composite) with ZrO_2 balls in a zirconia pod. The pod was filled with dry Ar gas, and the Cr and Si powders were used as received. The weight ratio of the balls to the sample was approximately 15:1. A high-energy planetary ball mill (P-6, Fritsch) was used for the MA process, which was performed at a rotary speed of 380 rpm and 30 °C for 25 h. We stopped the operation of the ball mill after 5 and 10 h of MA and stirred the samples. Other $LaSi_2$/MSi_2/Si (35/35/30 wt%; M = Mo, Nb, Ta, Ti, or W) nanocomposites were synthesized. The total MA times of $LaSi_2$/$MoSi_2$/Si, $LaSi_2$/$NbSi_2$/Si, $LaSi_2$/$TaSi_2$/Si, $LaSi_2$/$TiSi_2$/Si, and $LaSi_2$/WSi_2/Si were 20, 30, 30, 50, and 50 h, respectively. X-ray diffraction (XRD; Ultima IV, Rigaku) was performed at 5- or 10-h intervals after the beginning of the MA treatment. We determined that we had the target sample when the peak assigned to the two silicides appeared and the peak assigned to the raw materials disappeared. No peaks attributable to the impurity phase were observed. Therefore, the total MA time for each active material differed. The procedures were performed in an Ar-filled glove box (Miwa MFG, DBO-2.5LNKP-TS) with a dew point below –100 °C and an O_2 content below 1 ppm.

Electrode preparation.—We prepared $LaSi_2$/MSi_2/Si (M = Cr, Mo, Nb, Ta, Ti, or W) electrodes using the gas-deposition (GD) method.[42,43] This method does not require a binder or conductive additive; the electrode can only include the active material and current collector. This allows for the accurate evaluation of the basic electrochemical properties of the active material. Using GD method, the raw material powder was aerosolized with carrier gas in the conduit pipe and ejected from the nozzle at nearly the speed of sound against the substrate. The collision impact between the particles and substrate fractured and plastically deformed the particles. The surface of the particles created by the fracture faced the surface of other particles. Owing to the high-impact energy, the interdiffusion of atoms occurred at the interface. Thus, at room temperature, the particles strongly adhered to each other, resulting in mechanical durability and moderate electrical conductivity. This phenomenon is called "room-temperature impact consolidation."[44,45] Here, the $LaSi_2$/$CrSi_2$/Si nanocomposite was deposited on a current collector substrate of Cu foil (thickness = 20 μm). The detailed GD conditions have been reported.[10] The weight of the deposited nanocomposite samples was 100 ± 5 μg (elemental Si = approximately 30 μg). The minimum weighing capacity of the electronic balance used in this study was 1 μg; thus, the error in weight measurement was approximately 1%. The deposition amount per unit area was 0.509 and 0.153 mg cm^{-2} for nanocomposite and pure Si electrodes, respectively (the deposited area was 0.196 cm^2). For comparison, we fabricated a pure Si electrode through the GD method with a deposition weight of approximately 30 μg after subjecting the purchased Si powder at 380 rpm for 5 min. Figure S3 shows the particle-size distribution of the milled Si powder.

Coin-cell assembly and charge–discharge testing.—The prepared GD electrode was mounted in a 2032-type coin cell as the working electrode. A Li metal sheet (99.90%; thickness, 1 mm; Rare Metallic Co., Ltd.) and glass fiber filter (Whatman GF/A) were used as the counter electrode and separator, respectively. We used 1 mol dm^{-3} (M) lithium bis(fluorosulfonyl)amide (LiFSA Kishida Chemical Co., Ltd.) dissolved in *N*-methyl-*N*-propylpyrrolidinium bis(fluorosulfonyl)amide (Py13-FSA; Kanto Chemical Co., Inc.) as an ionic liquid electrolyte. High safety is required when handling high-energy-density LIBs incorporating Si-based anodes. Nonflammable electrolytes are essential for improving battery safety. We have investigated ionic liquids as electrolyte solvents because of their superior physicochemical properties[46–49] and reported that Si-based electrodes exhibit better electrochemical performances and ensure increased safety in certain ionic liquid electrolytes compared with typical organic liquid electrolytes.[10,26,29,39] The cell assembly and electrolyte preparation were performed in the Ar-filled glove box.

Galvanostatic charge–discharge tests were conducted using an electrochemical measurement system (HJ-1001SM8A, Hokuto Denko Co., Ltd.) at 30 °C. To form a good surface film on the electrode, which should exhibit high ionic and low electronic conductivities, precycling was performed. The electrode was charged from an open circuit voltage to 0.500 V at 0.1 *C*, maintained at 0.500 V for 12 h, and subsequently discharged to 2.000 V at 0.1 *C* (1 *C*: 3600 mA g^{-1}).[50] The potential range in the main tests was 0.005–2.000 V with a charging capacity limit of 1000 mA h g(*Si*)$^{-1}$. It is unlikely that all of the theoretical capacity of the Si electrode (3600 mA h g^{-1}) will be needed, considering the actual capacity of cathodes. Therefore, we limited the charging capacity to 1000 mA h g(*Si*)$^{-1}$, which is 3 times actual capacity of the graphite electrode currently used. Additionally, 1000 mA h g(*Si*)$^{-1}$ corresponded to 0.153 mA h cm(*active material*)$^{-2}$. The limitation was performed by controlling the charging time (approximately 17 min), whereas the discharging time was unlimited. The lithiation and delithiation were conducted in constant current mode. Here, the capacity of the silicides was ignored; the silicide-only and Si-only electrodes stored Li,[10,34,51,52] whereas the silicide in the silicide/Si composite electrodes did not exhibit charge–discharge capacity.[13]

Characterization.—The crystal structures of the prepared powders were analyzed by XRD. Al foil was used as the internal standard instead of Cu foil because the peaks of $CrSi_2$ overlapped with those of Cu. The XRD patterns were identified using the Inorganic Crystal Structure Database. The weight ratio of each composite sample was determined using an X-ray fluorescence (XRF) spectrometer (EDX-720, Shimadzu Corp.). The particle-size distribution of the synthesized powder was measured in an aqueous solution of 0.5 wt% sodium hexametaphosphate (SALD-2300, Shimadzu Corp.).

The cell was disassembled after the charge–discharge tests in the Ar-filled glove box. The dismounted electrode was washed with propylene carbonate and diethyl carbonate (Kishida Chemical Co., Ltd.) before drying. Thereafter, the electrode was introduced into the observation chamber of a field-emission scanning electron microscope (JSM-IT800, JEOL Co., Ltd.) or a scanning transmission electron microscope (JEM-ARM200F, JEOL Co., Ltd.) under non-atmospheric exposure using a transfer vessel. An electrode cross-section was prepared using a cross-section polisher (IB-19520CCP, JEOL Co., Ltd.) for scanning electron microscopy (SEM) and a focused ion beam (FIB) scanning electron microscope (SMF2000, Hitachi High-Tech Science Corp.) for transmission electron microscopy (TEM). SEM was performed with an acceleration voltage and a working distance of 10 kV and 10 mm, respectively. Energy-

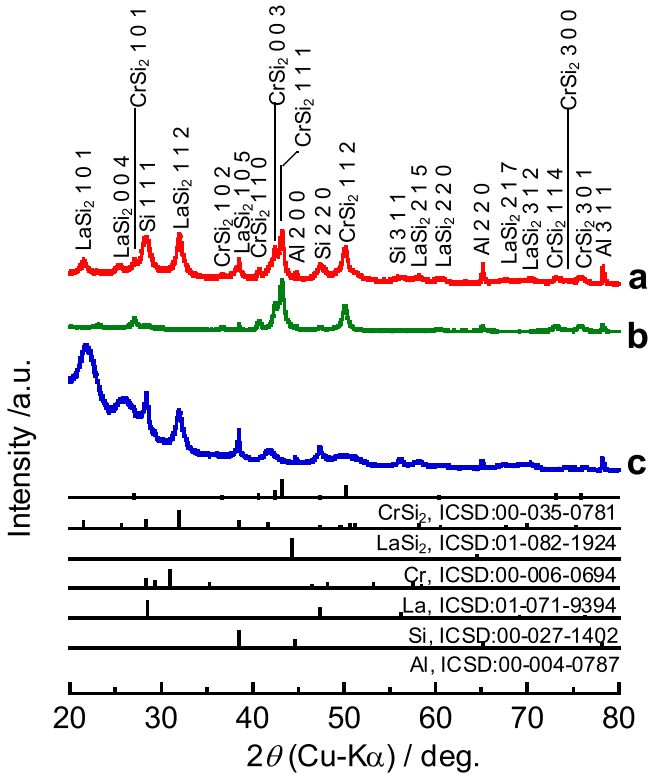

Figure 1. XRD patterns of powders synthesized from (a) elemental Cr, La, and Si by MA for 25 h, (b) elemental Cr and Si by MA for 40 h, and (c) elemental La and Si by MA for 5 h. The increase in the baseline in (c) was attributed to the Kapton film.

dispersive X-ray spectroscopy (EDS) was performed at 20 kV. A carbon layer was deposited on the electrode surface to protect it from damage using the Ga-ion beam of the FIB process. TEM was performed at 200 kV, and the ED spectra were recorded with 10 scans. Soft X-ray emission spectroscopy (SXES) was performed using a SXE spectrometer (SS-94000SXES) attached to the JSM-IT800 system. The EDS maps were superimposed using the Scanning Probe Image Processor (SPIP; ver. 5.1.1, Image metrology A/S). The black areas in the EDS maps of Cr and La were converted into white and superimposed. The yellow and blue colors of Cr and La, respectively, remained unchanged.

Results and Discussion

Characterization of synthesized powder.—Figure 1 shows the XRD patterns of the prepared powders. Figure 1a shows peaks assigned to $CrSi_2$, $LaSi_2$, and elemental Si, indicating the successful fabrication of the $LaSi_2/CrSi_2/Si$ nanocomposite despite the single-pod synthesis. For comparison, $CrSi_2/Si$ and $LaSi_2/Si$ composite samples were prepared (Figs. 1b and 1c), and their crystal structures are shown in Fig. S4. Table I lists the weight ratios of the composites. Their volume ratios were obtained using the measured weight ratios, which were close to the preparation values. Slight variations were observed owing to XRF measurement errors. The correct weight ratio was obtained by inductively coupled plasma atomic emission spectroscopy. The sample was mixed with hydrofluoric acid to dissolve Si. However, a white precipitate (probably LaF_3) was formed if the sample contained La, and the elemental concentration would not be accurately determined.

Figure 2 shows the particle-size distribution of the composite samples measured in an aqueous solution of 0.5 wt% sodium hexametaphosphate, along with the D_{10}, D_{50}, and D_{90} values. Figure 3 shows the SEM images of these composite powders. The results showed that the secondary particles of $LaSi_2/CrSi_2/Si$ were larger than those of $CrSi_2/Si$ and $LaSi_2/Si$. In addition, the primary particles of each composite were within the submicron range.

Table I. Weight and volume ratios of $LaSi_2/CrSi_2/Si$, $CrSi_2/Si$, and $LaSi_2/Si$ nanocomposite powders.

Composite	Preparation ratio/ wt%	Measured ratio/ wt%	Volume ratio/ vol%
$LaSi_2/CrSi_2/Si$	35/35/30	39/27/33	29/19/52
$CrSi_2$	70/30	74/26	57/43
$LaSi_2$	70/30	60/40	41/59

*Weight ratio was investigated by XRF.

**Volume ratio was estimated using the weight ratio and density. The densities of $LaSi_2$, $CrSi_2$, and Si were 5.14, 5.02, and 2.33 g cm^{-3}, respectively.

Charge–discharge behavior of $LaSi_2/CrSi_2/Si$ nanocomposite electrode.—Figure 4 shows the 1st, 2nd, 100th, 600th, and 1200th charge–discharge curves of the nanocomposite electrodes and the curve of the cycle where the CE reached 99.0%. The pure Si electrode exhibited potential plateaus at approximately 0.1 and 0.4 V on the charge and discharge curves, attributable to the lithiation and delithiation of Si, respectively. The $LaSi_2/CrSi_2/Si$ and $LaSi_2/Si$ nanocomposite electrodes exhibited the same lithiation behavior as the pure Si electrode on the charge side and a 0.1 V higher potential plateau on the discharge side during the first and second cycles. There are two reasons for this difference. First, an overpotential may have occurred; if so, the plateau potential on the charge side should be lower than that of the Si electrode. However, this was unlikely because the potentials were practically identical. Second, the capacity was attributed to the silicide in the composite. We reported that pure silicide electrodes exhibited higher lithiation–delithiation plateaus and/or slopes than Si electrodes.[51–53] However, the silicide phase in the composite electrode hardly stored Li (although it may have functioned as a Li-diffusion path).[13,54] Table S1 lists Li^+ diffusion coefficients (D_{Li+}) of Si and certain silicides estimated using a galvanostatic intermittent titration technique.[10] The D_{Li+} of the silicides was an order of magnitude higher than that of Si. Assuming that $CrSi_2$ and $LaSi_2$ stored Li in the $LaSi_2/CrSi_2/Si$ and $LaSi_2/Si$ electrodes, the plateau potential on the charge side should have exceeded than that of the Si electrode; however, they were practically identical. Thus, the difference in the aforementioned reaction behavior had not been clarified at this stage. However, the Si environment may have had a certain influence, as described below.

Prior to 100th cycle, the $CrSi_2/Si$ electrode exhibited a high potential plateau and slope on the charge and discharge sides, respectively. We assumed that the $CrSi_2$ phase in the composite electrode stored and released Li, although the plateau and slope potentials decreased as the cycle proceeded (Figs. 4a–4d). After 1200 cycles, the behavior of the $CrSi_2/Si$ electrode was practically identical to that of the Si electrode (Fig. 4e). It is possible that a part of the electrode collapsed and the active material was no longer involved in the charge–discharge process. However, it was unlikely that only $CrSi_2$ was electrically isolated and not simultaneously storing Li. The metallographic structure of the $CrSi_2/Si$ electrode did not change before and after 1200 cycles (Fig. S1). However, changes in the physicochemical and/or mechanical properties of $CrSi_2$ were unclear from the image. The properties that were prominent during the charge–discharge cycling might have affected the curve. Figure S5 shows the CEs of the electrodes during the initial cycles. The precycling was similar for all the electrodes. However, the pure Si electrode exhibited the highest initial CE, and the three composite electrodes exhibited lower CEs owing to the additional electrolyte decomposition on the surface of the silicide with high electrical conductivity. The CEs of the four electrodes reached 99.0% at the 20th cycle (Fig. 4f).

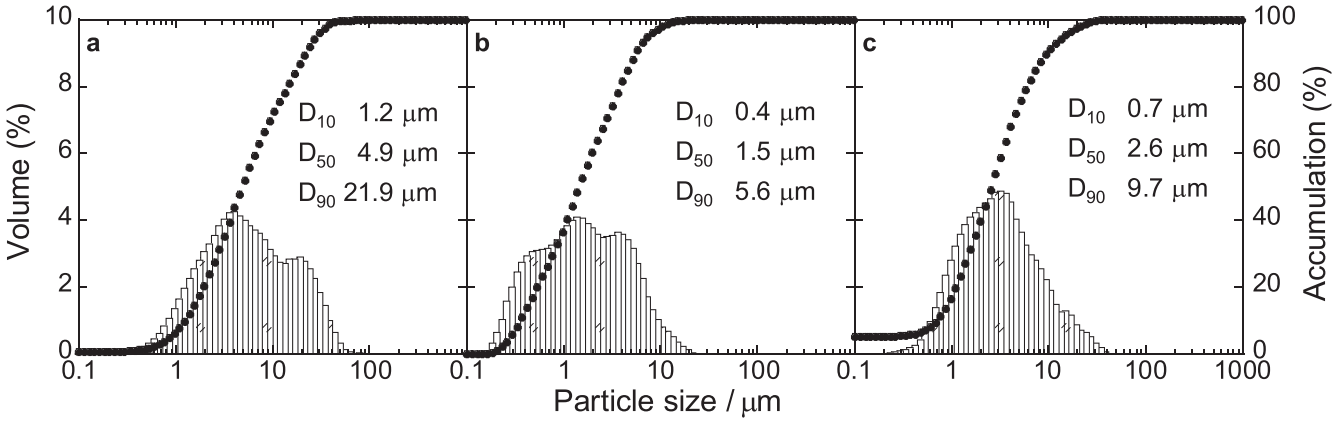

Figure 2. Particle-size distribution of (a) $LaSi_2/CrSi_2/Si$, (b) $CrSi_2/Si$, and (c) $LaSi_2/Si$ powders measured in an aqueous solution of 0.5 wt% sodium hexametaphosphate.

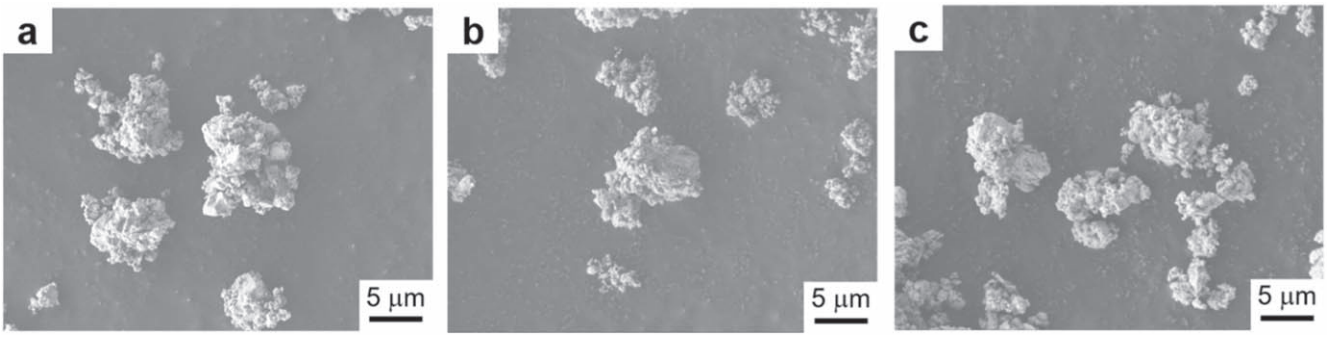

Figure 3. SEM images of (a) $LaSi_2/CrSi_2/Si$, (b) $CrSi_2/Si$, and (c) $LaSi_2/Si$ powders.

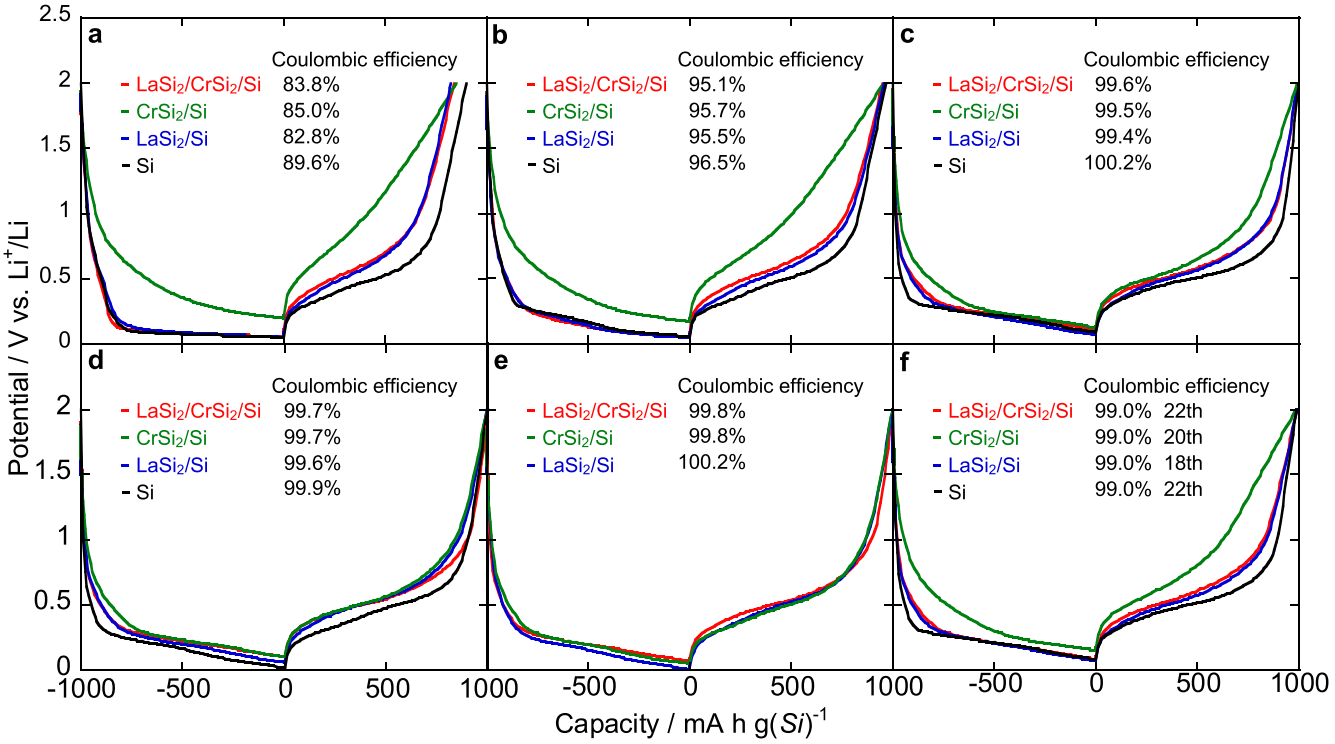

Figure 4. Charge–discharge curves of $LaSi_2/CrSi_2/Si$, $CrSi_2/Si$, $LaSi_2/Si$, and Si electrodes at the (a) 1st, (b) 2nd, (c) 100th, (d) 600th, and (e) 1200th cycles and (f) the cycle where the Coulombic efficiency reached 99.0%.

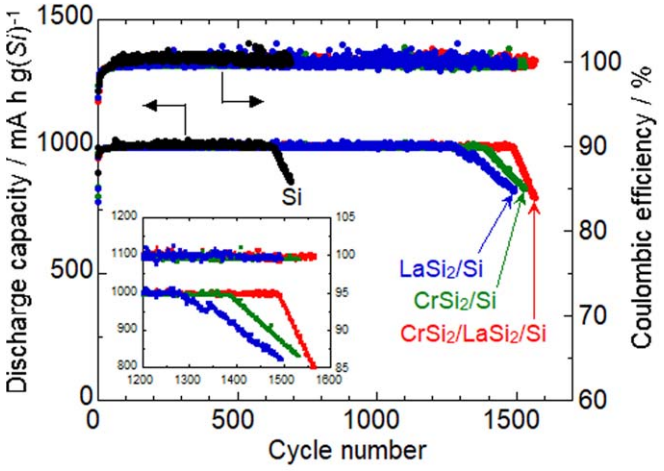

Figure 5. Cycle lives of $LaSi_2/CrSi_2/Si$, $CrSi_2/Si$, $LaSi_2/Si$, and Si electrodes in 1 M LiFSA/Py13-FSA with a charge capacity limitation of 1000 mA h g^{-1} at 1 *C* per unit weight of elemental Si.

Figure 5 shows the cycle lives of the $LaSi_2/CrSi_2/Si$, $CrSi_2/Si$, $LaSi_2/Si$, and pure Si electrodes under a charge capacity limitation of 1000 mA h $g(Si)^{-1}$. The CE data are also shown. The three nanocomposite electrodes exhibited a longer cycle life than the pure Si electrode. The $CrSi_2/LaSi_2/Si$ electrode exhibited the longest life among the composite electrodes. It is believed that charging and discharging causes repeated expansion and construction of the Si-based electrodes, increasing the amount of Si that cannot collect current. When the Si that can collect current could no longer carry a capacity of 1000 mA h $g(Si)^{-1}$, the discharge capacity would fade. The difference between the cycle lives of the electrodes was approximately 100 cycles, and a reproducibility within a maximum of 50 cycles was confirmed for each electrode (Fig. S6). The cycle life significantly improved when silicides of different stiffnesses (hardnesses) were employed instead of $CrSi_2$, as described below. TEM revealed whether the metallographic structure changed because of the addition of $CrSi_2$ or not. The high-rate performance of the $LaSi_2/CrSi_2/Si$ electrode was virtually the same as that of the $LaSi_2/Si$ and $CrSi_2/Si$ electrodes (Fig. S7), indicating that the electrical conductivities of silicides were almost identical.

Changes in metallographic structure before and after charge–discharge cycles.—Figure 6 shows a bright-field (BF) TEM image, a high-resolution (HR) BF-TEM image, and the corresponding EDS maps of a $LaSi_2/CrSi_2/Si$ nanocomposite particle prior to charge–discharge cycling. Figure S8 shows the corresponding selected area electron diffraction (SAED) and d-spacings based on the SAED analysis. The lattice fringe analysis in the HR BF-TEM image (Fig. 6b) revealed that the $CrSi_2$, $LaSi_2$, and elemental Si were homogeneously mixed at the nanoscale level. The existence of these phases is confirmed in Fig. S8. However, it is difficult to infer the type of metallographic structure formed by the silicide and elemental Si from Figs. 6a–6e. Thus, we determined the structure by superimposing the EDS maps of Cr and La (Fig. 6f) and observed that the Si phase (with a diameter of several tens of nanometers) was surrounded by $CrSi_2$ and $LaSi_2$.

Figure 7 shows the BF-TEM and HR BF-TEM images, corresponding EDS maps, and superimposed image of the $LaSi_2/CrSi_2/Si$ nanocomposite electrode after the 1200th cycle. Figure S9 shows the results after the 600th cycle. The Si phase was highly dispersed in the silicide matrix phase. Although microstructural inversion only occurred for the $LaSi_2/Si$ electrode,[39] the addition of $CrSi_2$ to the $LaSi_2/Si$ composite suppressed the changes in the metallographic structure after long-term cycling. The stiff $CrSi_2$ is known to function as a support framework, improving the structural stability of the whole electrode and preventing microstructural inversion. Thus, the superior cycle life was achieved because of the synergistic effect of $LaSi_2$ and $CrSi_2$. The elasticity of $LaSi_2$ relaxed the Si-generated stress, and the stiffness of $CrSi_2$ withstood the Si-generated stress and maintained the metallographic structure. The particle size of the elemental Si remained unchanged before and after the charge–discharge cycling. Although it is well known that crystalline Si (*c*-Si) changes into amorphous Si (*a*-Si) after charge–discharge cycles, the presence of *c*-Si was confirmed after the long-term cycle test. Considering that not all the *c*-Si in the electrode stored Li with the charge capacity limitation of 1000 mA h g^{-1}, unreacted Si microcrystals were observed (Fig. 7).

Figure S10 shows low-magnification TEM images of the composite electrodes before and after charge–discharge cycling. The microstructural changes in $LaSi_2/Si$ and the maintenance of the $LaSi_2/CrSi_2/Si$ and $CrSi_2/Si$ microstructures after 1200 cycles were observed even at a low magnification. For the $LaSi_2/CrSi_2/Si$ electrode, a drastic microstructural change (i.e., a reversal between the silicide and Si phases) occurred after 1700 cycles, where capacity fading was observed. Contrarily, for the $LaSi_2/Si$ electrode, microstructural changes were observed after 600 cycles, earlier than where the capacity degradation occurred. These results highlight various mechanisms for the degradation of silicide/Si composite electrodes. Microstructural changes should not necessarily degrade capacity (subsequently discussed).

Change in electrode thickness and phase transition during charge–discharge cycling.—Figure 8 shows the cross-sectional SEM images of the $CrSi_2/Si$, $LaSi_2/Si$, and $LaSi_2/CrSi_2/Si$ electrodes before and after charge–discharge cycling. The thickness of the active material layer was approximately 3 μm prior to cycling. Differences in thickness were observed at the 600th cycle. The thickness of the $LaSi_2/Si$ electrode reached 23 μm at the 1200th cycle, and the increase in thickness of the $CrSi_2/Si$ electrode was suppressed to approximately half of that of the $LaSi_2/Si$ electrode. The thickness of the $LaSi_2/CrSi_2/Si$ electrode was suppressed to approximately one-third that of the $LaSi_2/Si$ electrode.

Figure 9a shows the cycle dependence of the relative thickness (t/t_0) of the $CrSi_2/Si$, $LaSi_2/Si$, and $LaSi_2/CrSi_2/Si$ electrodes. The corresponding thicknesses are shown in Fig. S11. The pure Si electrode maintained a t/t_0 of approximately 1.5 over 300 cycles; however, the t/t_0 reached 8.3 at the 600th cycle prior to capacity fading.[10] The t/t_0 of the $LaSi_2/Si$ electrode rapidly increased after 600 cycles, where the inversion of the metallographic structure was observed.[39] Although the t/t_0 of the $CrSi_2/Si$ electrode rapidly increased after 600 cycles, no microstructural inversion was observed (Figs. S1 and S2). We previously reported that the t/t_0 of the $LaSi_2/Si$ electrode reached approximately 3 during the first 20 cycles.[39] This was higher than that obtained in the present study owing to the different conditions of the charge–discharge cycling test. Here, precycling was performed to form a good surface film, and the cycling test was performed at 1.0 *C*. However, in the previous study, precycling was not performed, and the cycling test was performed at 0.4 *C*. Thus, the t/t_0 varies across studies. Although the increase in the t/t_0 of the $CrSi_2/Si$ and $LaSi_2/Si$ electrodes was suppressed at the 600th cycle, the t/t_0 reached approximately 6.8 at the 1200th cycle.

The t/t_0 of the $LaSi_2/CrSi_2/Si$ electrode remained unchanged during the first 200 cycles and was a lower than those of the $CrSi_2/Si$, $LaSi_2/Si$, and Si electrodes over 1200 cycles. The combination of the two silicides resulted in different electrode thicknesses despite having the same Li storage contents. Previously, we reported that the expansion of Si-based electrodes is dependent on the amount of the Li-rich phase formed, which has a large expansion ratio of 280%, and Li distribution in the Si layer.[10,27] The former was studied based on a differential capacity (dQ/dV) plot obtained by differentiating the discharge curve with respect to potential (voltage), and the latter was investigated using our SXES-based analysis method.

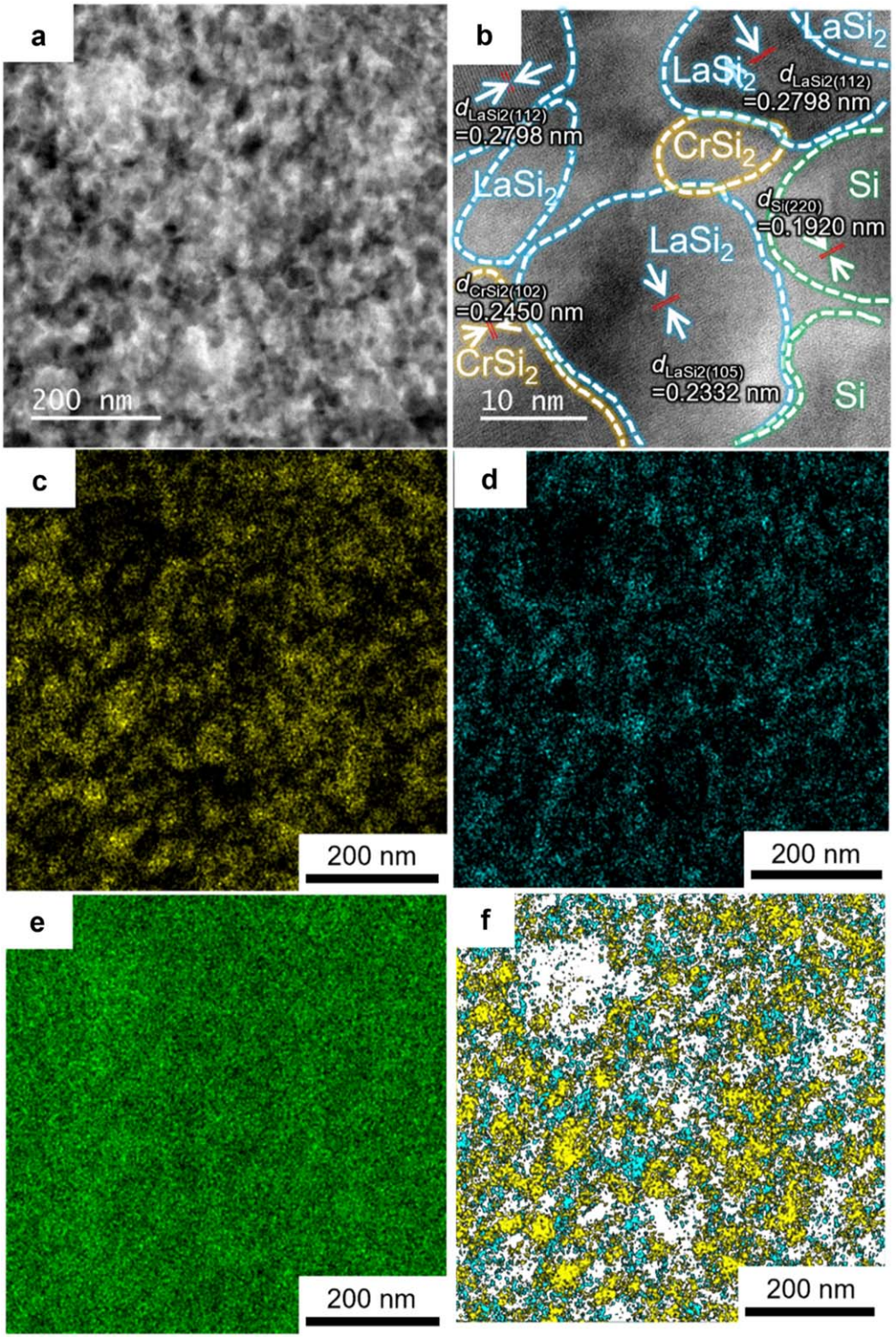

Figure 6. (a) BF-TEM and (b) HR BF-TEM images of $LaSi_2/CrSi_2/Si$ composite powder prior to charge–discharge cycling and corresponding EDS maps for (c) Cr, (d) La, and (e) Si. (f) Overlaid view of Cr (yellow) and La (blue); the black areas were inverted into white areas, which denote elemental Si.

Figure S12 shows the SXE spectra of the pure Si and $LaSi_2$ electrodes prior to charge–discharge cycling. In the Si spectrum, a peak at approximately 90 eV was attributed to a low-lying 3 s state. In contrast, a peak and a broad shoulder at approximately 92 and 96 eV, respectively, were attributed to the p components of the sp^3 hybrid orbital. In the $LaSi_2$ spectrum of, a peak at approximately 80 eV was assigned to La, and two peaks around 90 and 98 eV were attributed to Si. The spatial resolution of SXES was approximately 1 μm, and SXES revealed that the silicides and elemental Si phases were mixed at the nanoscale level. Although we ignored the capacities of $CrSi_2$ and $LaSi_2$, Li can pass through silicides. Thus, the SXE spectrum of the silicides may have changed after the charge–discharge tests. Consequently, it was difficult to clarify the distribution of Li in the nanocomposite electrodes by SXES. Thus, we investigated the amount of the Li-rich phase formed using the dQ/dV plot of the electrode.

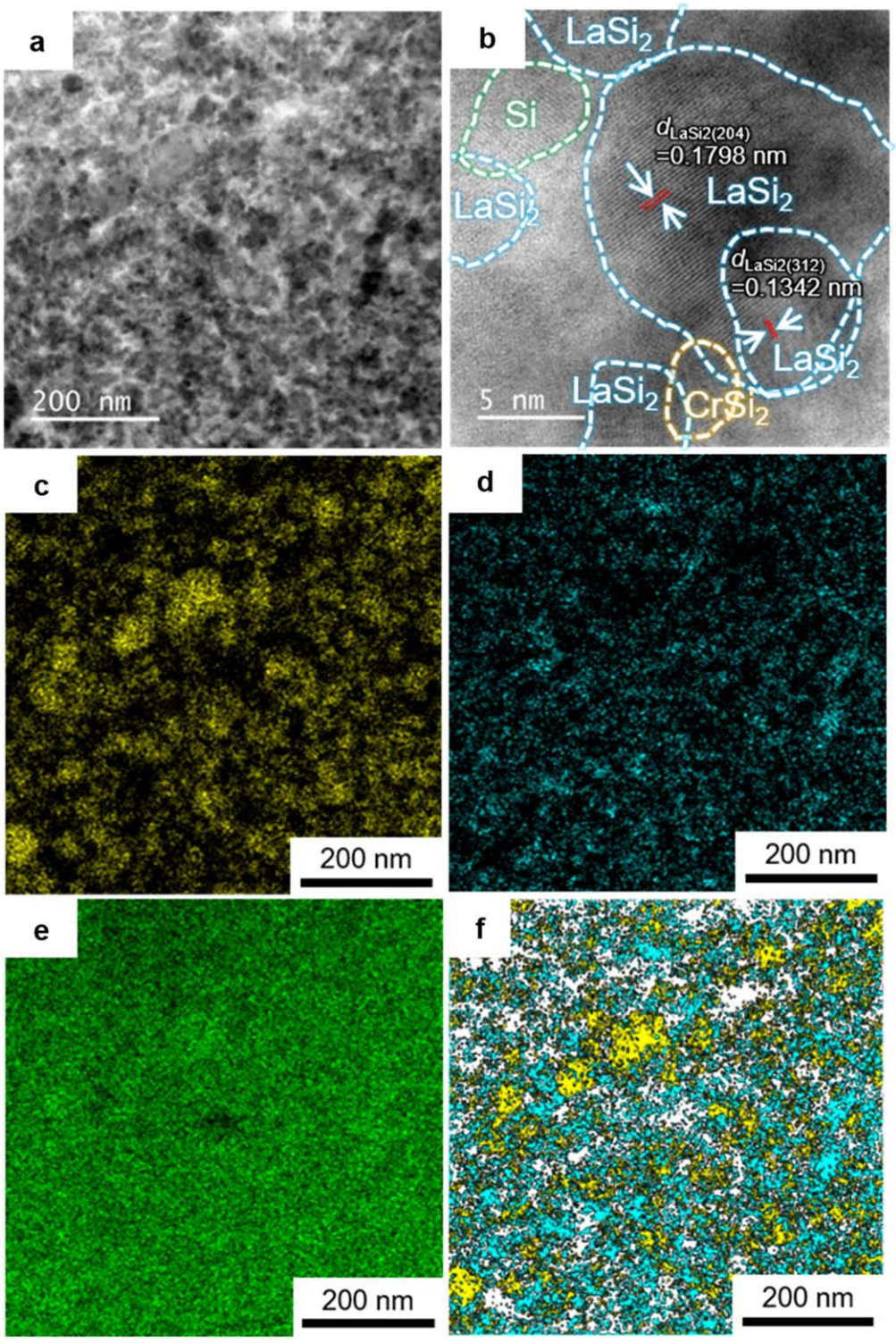

Figure 7. (a) BF-TEM and (b) HR BF-TEM images of $LaSi_2/CrSi_2/Si$ composite electrode after the 1200th cycle and corresponding EDS maps for (c) Cr, (d) La, and (e) Si. (f) Overlaid view of Cr (yellow) and La (blue); the black areas were inverted into white areas, which denote elemental Si.

Figure 9b shows the change in the amount of the amorphous Li-rich (*a*-Li-rich) phase formed with the cycle number estimated from the dQ/dV plot (Figs. S13–S16). As the crystalline Li-rich phase is rarely formed electrochemically, we investigated the amount of the *a*-Li-rich phase. The amount formed on the composite electrodes was lower than that on the pure Si electrode. The differences in the amounts of the *a*-Li-rich phase, despite having the same Li contents, indicated that the Li distribution was heterogeneous in the active material layer. Owing to the higher electronic and Li-ion conductivities of the silicides compared with those of pure Si, we assumed that Li was distributed throughout the entire composite electrode and that the formation of the *a*-Li-rich phase was suppressed.

Prior to the 600th cycle, the largest amount of the *a*-Li-rich phase was formed on the $LaSi_2/Si$ electrode, followed by the $LaSi_2/CrSi_2/Si$ and $CrSi_2/Si$ electrodes. The $CrSi_2$ phase was finely dispersed in the Si matrix (Fig. S1). However, there might have been

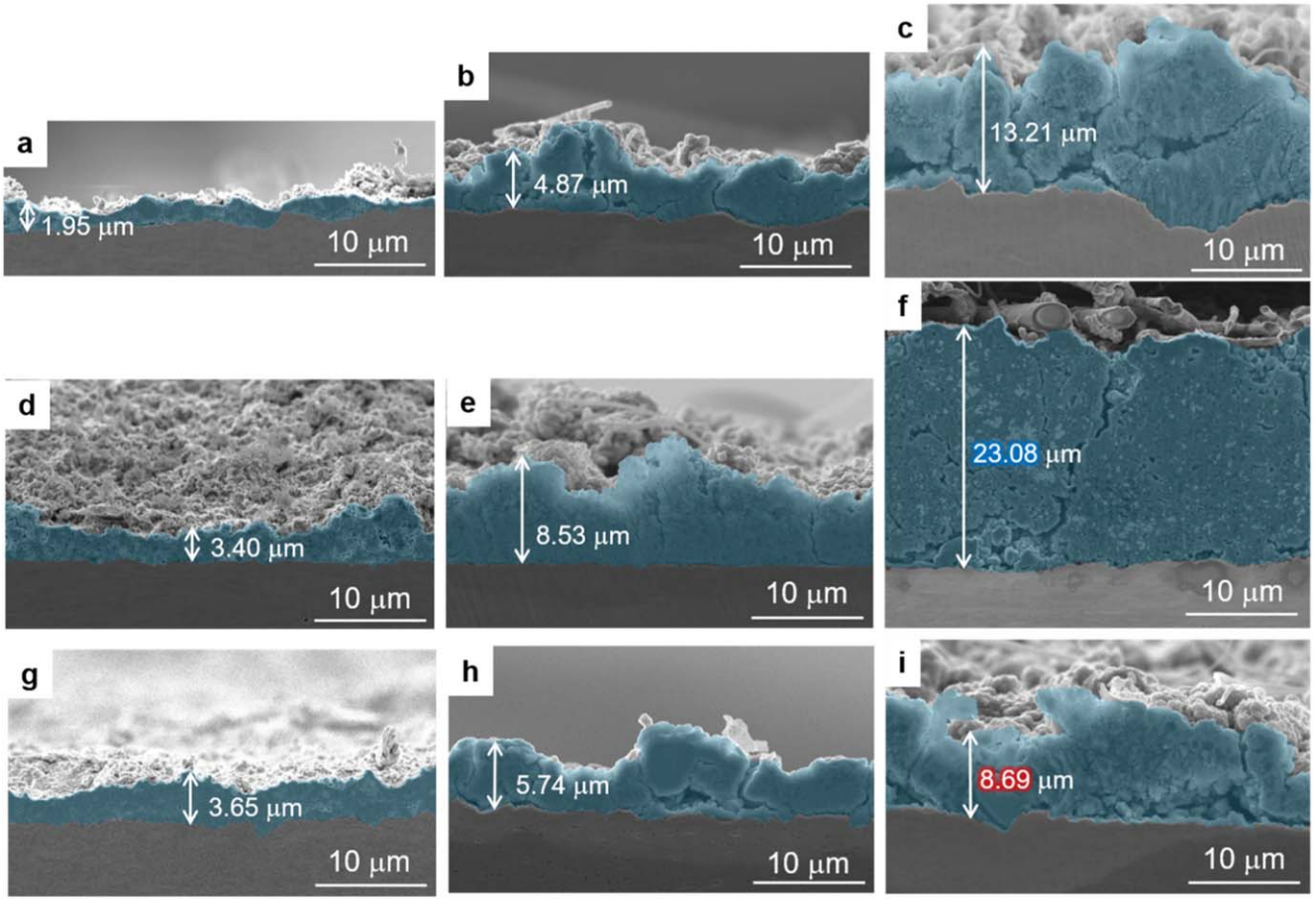

Figure 8. Cross-sectional SEM images of (a–c) $CrSi_2$/Si, (d–f) $LaSi_2$/Si, and (g–i) $LaSi_2$/$CrSi_2$/Si electrodes. The images were obtained before (a, d, and g) and after 600 (b, e, and h) and 1200 cycles (c, f, and i).

microscopic areas where stiff $CrSi_2$ surrounded Si because $CrSi_2$ was more abundant in terms of the volume ratio (Table I). In such areas, even if Si stored Li, it could not expand outward because of the presence of stiff $CrSi_2$. Thus, Li could not remain close to the Si surface, and the *a*-Li-rich phase could not form but had to move inside the Si. Thus, the *a*-Li-rich phase on the $CrSi_2$/Si electrode was considered to be the smallest. Owing to such an effect, the amount of the *a*-Li-rich phase formed on the $LaSi_2$/$CrSi_2$/Si electrode was lower than that in the $LaSi_2$/Si electrode.

After 600 cycles, the slopes of the $LaSi_2$/Si and $CrSi_2$/Si electrodes steepened, whereas that of the $LaSi_2$/$CrSi_2$/Si electrode remained unchanged (Fig. 9b). The metallographic change in $LaSi_2$/Si, which occurred after the 600th cycle, rendered it impossible to relax the Si-generated stress,[39] resulting in a rapid increase in the t/t_0 (Fig. 9a). Fine cracks were observed in the $CrSi_2$/Si electrode layer after 600 cycles (Fig. S10f). This was probably because $CrSi_2$ could not withstand the Si-generated stress owing to the repeated charge–discharge cycles. The amount of the *a*-Li-rich phase formed increased because the active materials were electrically isolated owing to the occurrence of cracks, and Li was stored in the remaining Si, leading to a rapid increase in the t/t_0. The slope of the $LaSi_2$/$CrSi_2$/Si electrode remained unchanged because the metallographic structure did not change and there was no electrical isolation.

Effect of differences in silicide stiffness on cycle life.—The introduction of $CrSi_2$, which exhibits stiffness, into $LaSi_2$/Si nanocomposites, where microstructural changes occur, suppressed changes in the metallographic structure and improved the charge–-discharge cycle life. This study investigated the effect of different silicide stiffnesses on the cycle life. Figure 10a shows the cycle lives of the $LaSi_2$/MSi_2/Si (where M = Cr, Mo, Nb, Ta, Ti, or W) electrodes with a charge capacity limit of 1000 mA h g$(Si)^{-1}$. Furthermore, the Vickers hardness of MSi_2 was demonstrated.[55] The XRD pattern, particle-size distribution, and high-magnification SEM results of $LaSi_2$/MSi_2/Si are shown in Figs. S17–S19, respectively. It can be seen that the $LaSi_2$/MSi_2/Si nanocomposites were successfully prepared, the D_{50} value was in the range of 3 to 5 μm, and each phase was uniformly mixed. The weight ratios of the composites are presented in Table S2, and their volume ratios were obtained using the measured weight ratios. Many of the synthesized powders had almost the same weight ratios as the preparation values, whereas the weight ratios of the Ta-containing samples ($LaSi_2$/$TaSi_2$/Si and $TaSi_2$/Si) significantly differed from the initial values. This was because the characteristic X-rays of Ta ($M\alpha_1$ line: 1.71 keV) and Si ($K\alpha$ line: 1.74 keV) overlapped and could not be accurately measured. In addition, $MoSi_2$/Si could not be synthesized by MA under the present conditions. Consequently, α-$MoSi_2$ and β-$MoSi_2$ were formed. Figures S20–S24 show the charge–discharge curves of the $LaSi_2$/MSi_2/Si (M = Cr, Mo, Nb, Ta, Ti, or W) electrodes. For comparison, the results of the MSi_2/Si, $LaSi_2$/Si, and pure Si electrodes were considered, and the phenomena shown in Fig. 4 were identified.

The cycle life was the shortest when WSi_2, with the highest stiffness (highest Vickers hardness), was added. The cycle life improved with a decrease in the stiffness of MSi_2 (low Vickers hardness). Superior cycling performance was achieved when $NbSi_2$ was added, maintaining a reversible capacity of 1000 mA h g$(Si)^{-1}$ for approximately 1800 cycles. Contrarily, the cycle life decreased when $TiSi_2$, which exhibits the lowest stiffness, was used. Figure 10b shows the correlation between the Vickers hardness of the stiff silicide and the cycle life of nanocomposite electrodes

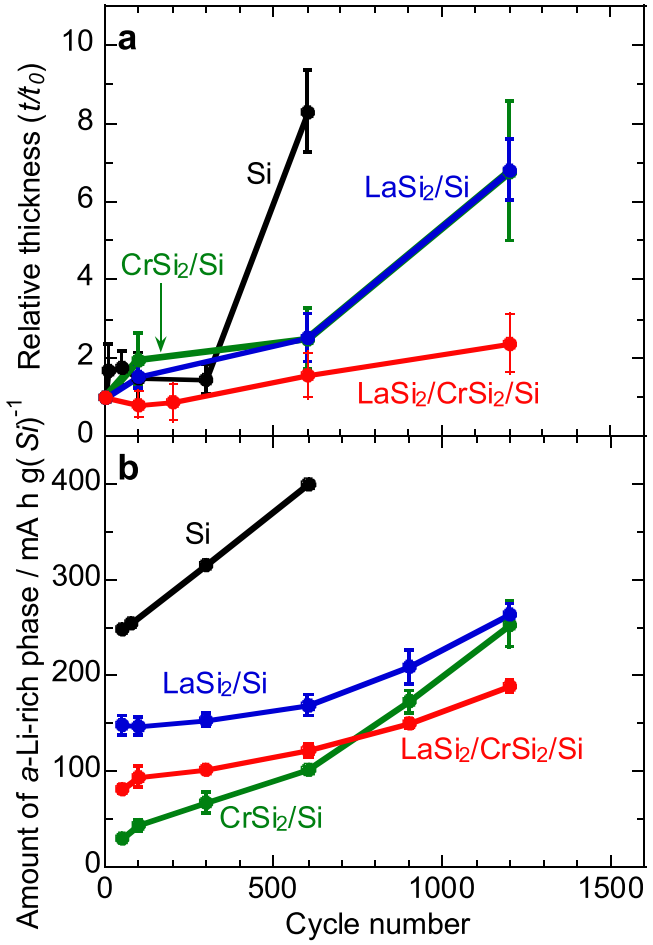

Figure 9. Changes in the (a) relative thickness (t/t_0) and (b) the amount of the *a*-Li-rich phase of each electrode with cycle number. t_0 and t represent the thickness before and after cycling, respectively. The value of t was investigated in the lithiation state. The formed amount indicates the peak area of the *a*-Li-rich phase estimated by peak fitting each dQ/dV plot (Figs. S13–S16).

containing $LaSi_2$, silicides with varying stiffnesses, and elemental Si. The cycle life increased with a decrease in the Vickers hardness, and the longest cycle life was obtained at approximately 9 GPa. Conversely, the cycle life decreased with a decrease in hardness. This trend was observed when $LaSi_2$ was adopted as the elastic silicide, and the same trend may not have been observed with other elastic silicides. Additionally, Fig. S25 shows the relationship between the weight of active material and the number of cycles before the discharge capacity begins to drop below 1000 mA h g^{-1}. The lower the amount of active material deposited, the less stress is generated in the active material layer, which can improve the cycle life. However, no such correlation was observed.

Figure 11 compares the cycle lives of the $LaSi_2/MSi_2$/Si, MSi_2/Si, $LaSi_2$/Si, and pure Si electrodes. The capacity degradation of the $LaSi_2/WSi_2$/Si electrode occurred between cycles where the capacity degradation of the WSi_2/Si and $LaSi_2$/Si electrodes was confirmed. Therefore, no synergistic effect of stiff WSi_2 and elastic $LaSi_2$ was achieved. For the $LaSi_2/MoSi_2$/Si electrode, we could not determine if the synergistic effect was achieved because $MoSi_2$/Si could not be synthesized. Contrarily, the cycle lives of the $LaSi_2/TaSi_2$/Si, $LaSi_2/TiSi_2$/Si, and $LaSi_2/NbSi_2$/Si electrodes were superior to those of the MSi_2/Si and $LaSi_2$/Si electrodes, indicating that the synergistic effect was achieved. Although the $NbSi_2$/Si electrode exhibited a cycle life comparable to that of the pure Si electrode, the best performance was obtained by combining it with $LaSi_2$. Thus, a high synergistic effect was obtained for the $LaSi_2/NbSi_2$/Si electrode.

Reaction behaviors of $LaSi_2/MSi_2$/Si electrodes.—Figure 12 shows the change in the amount of the *a*-Li-rich phase of the $LaSi_2/MSi_2$/Si nanocomposite electrodes (M = Cr, Mo, Nb, Ta, Ti, or W) formed over the cycle. Although the difference in the amounts was not confirmed before the 600th cycle, the amount began to vary after 900 cycles. After 1200 cycles, more a-Li-rich phase was formed on the $LaSi_2/WSi_2$/Si and $LaSi_2/TaSi_2$/Si electrodes, with relatively poor cycle lives. However, less *a*-Li-rich phase was formed on the $LaSi_2/MoSi_2$/Si and $LaSi_2/NbSi_2$/Si electrodes. The latter two electrodes exhibited superior performance owing to suppressed Si expansion and electrode collapse. Although the performance of the $LaSi_2/CrSi_2$/Si and $LaSi_2/TiSi_2$/Si electrodes differed, the amounts of *a*-Li-rich phase formed were practically the same, suggesting a difference in Li distribution.

Figure S26 shows the variation in the amounts of the *a*-Li-rich phase formed on the $LaSi_2/MSi_2$/Si, MSi_2/Si, $LaSi_2$/Si, and pure Si (M = Cr, Mo, Nb, Ta, Ti, or W) electrodes with the cycle number. The *a*-Li-rich phase of the $LaSi_2/MSi_2$/Si electrode was less than that of the $LaSi_2$/Si electrode in all the cycles regardless of the element of M. Although the *a*-Li-rich phase of the MSi_2/Si electrode was less than that of the $LaSi_2/MSi_2$/Si electrode early in the cycles, it exceeded those of the $LaSi_2/MSi_2$/Si and $LaSi_2$/Si electrodes after

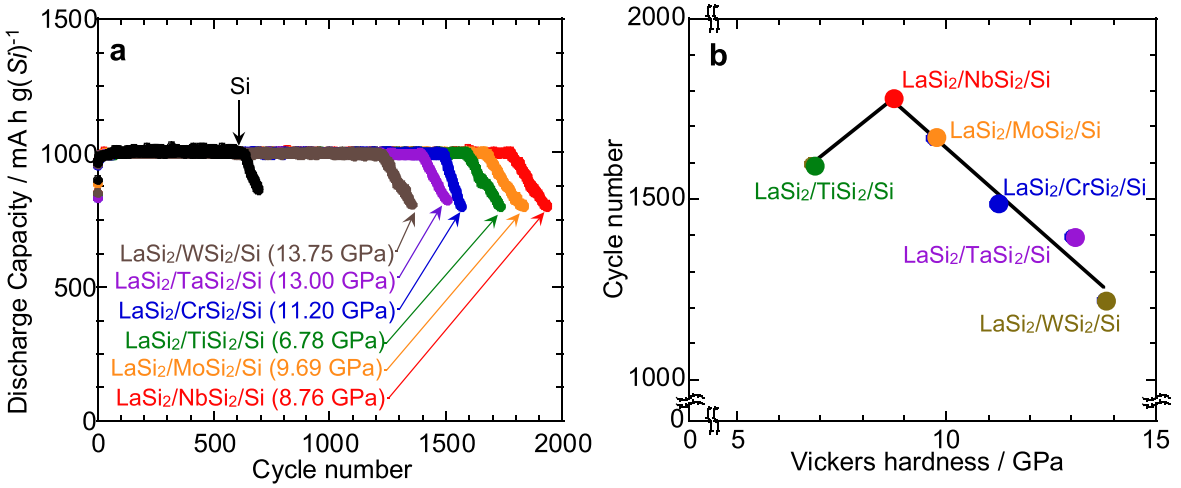

Figure 10. (a) Cycle lives of $LaSi_2/MSi_2$/Si composite electrodes (M = Cr, Mo, Nb, Ta, Ti, or W) in 1 M LiFSA/Py13-FSA with a charge capacity limitation of 1000 mA h g^{-1} at 1 *C* per unit weight of elemental Si. The values in parentheses denote the Vickers hardness of MSi_2. (b) Correlation between the Vickers hardness of stiff silicide and the cycle lives of composite electrodes containing various stiff silicides, $LaSi_2$, and elemental Si.

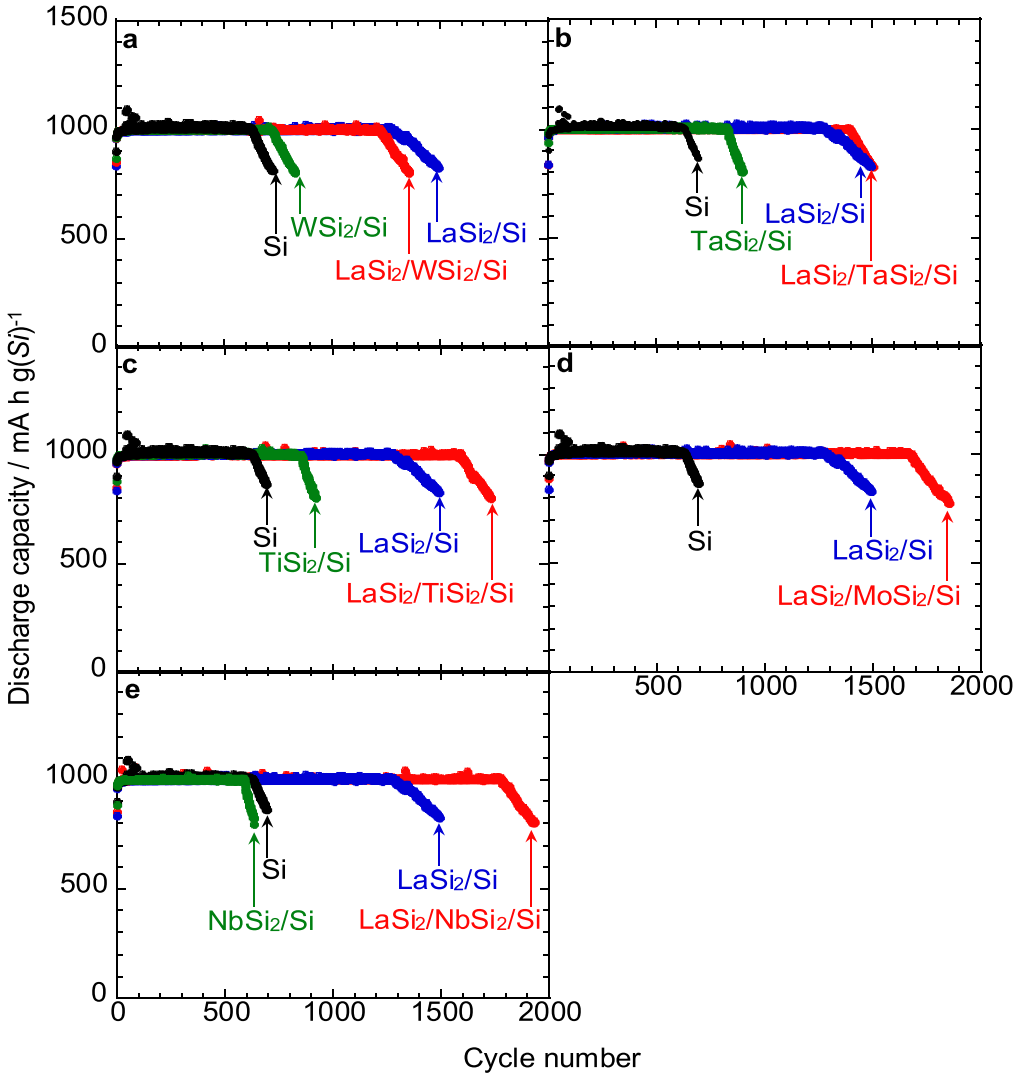

Figure 11. Cycle lives of $LaSi_2/MSi_2/Si$ composite electrodes, where M = (a) W, (b) Ta, (c) Ti, (d) Mo, and (e) Nb in 1 M LiFSA/Py13-FSA with a charge capacity limitation of 1000 mA h g^{-1} at 1 *C* per unit weight of elemental Si. The results of MSi_2/Si, $LaSi_2/Si$, and pure Si electrodes are shown.

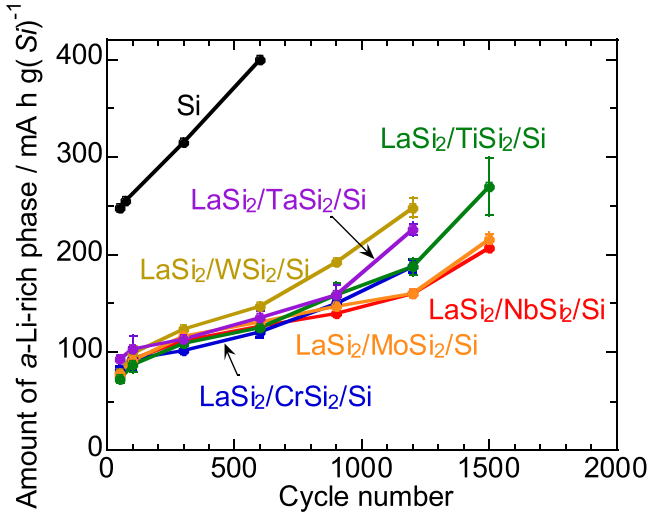

Figure 12. Changes in the amount of *a*-Li-rich phase formed on the $LaSi_2/MSi_2/Si$ composite electrodes (M = Cr, Mo, Nb, Ta, Ti, or W) with the cycle number. The results for the pure Si electrode are illustrated. The amount formed indicates the peak area of the *a*-Li-rich phase estimated by peak fitting each dQ/dV plot.

cycling (M = W, Ta, or Nb). The final amount of the *a*-Li-rich phase formed on the $TiSi_2/Si$ and $CrSi_2/Si$ electrodes was comparable to that formed on the $LaSi_2/Si$ electrode.

Figure S27 shows the overlaid views of the EDS maps of the $LaSi_2/WSi_2/Si$, $LaSi_2/CrSi_2/Si$, and $LaSi_2/MoSi_2/Si$ electrodes. Prior to charge–discharge cycling, the Si phase (with a diameter of several tens of nanometers) was surrounded by a stiff silicide (WSi_2, $CrSi_2$, or $MoSi_2$) and $LaSi_2$. This indicated that its metallographic structure virtually remained the same, regardless of the stiff silicide. After the 600th and 1200th cycles, no microstructural inversion was observed. No differences were observed in the microstructure of the electrodes; thus, we obtained low-magnification BF-TEM images (Fig. 13). After 600 cycles, the $LaSi_2/MoSi_2/Si$ electrode with a relatively long cycle life exhibited more cracks than the $LaSi_2/CrSi_2/Si$ electrode with a medium cycle life (similar to the $LaSi_2/WSi_2/Si$ electrode with the shortest cycle life). After 1200 cycles, both electrodes exhibited the further formation of fine cracks. No significant cracks were observed on the $LaSi_2/CrSi_2/Si$ electrode until the 1200th cycle. After 1700 cycles, when the capacity fading of the $LaSi_2/CrSi_2/Si$ electrode was observed, many fine cracks were observed. Three electrodes maintained a discharge capacity of 1000 mA h $g(Si)^{-1}$ up to 1200 cycles, implying that the aforementioned cracks were not directly related to capacity decay. Figure 13 show that other mechanical properties, such as fatigue life and fracture toughness, may have influenced electrode collapse.

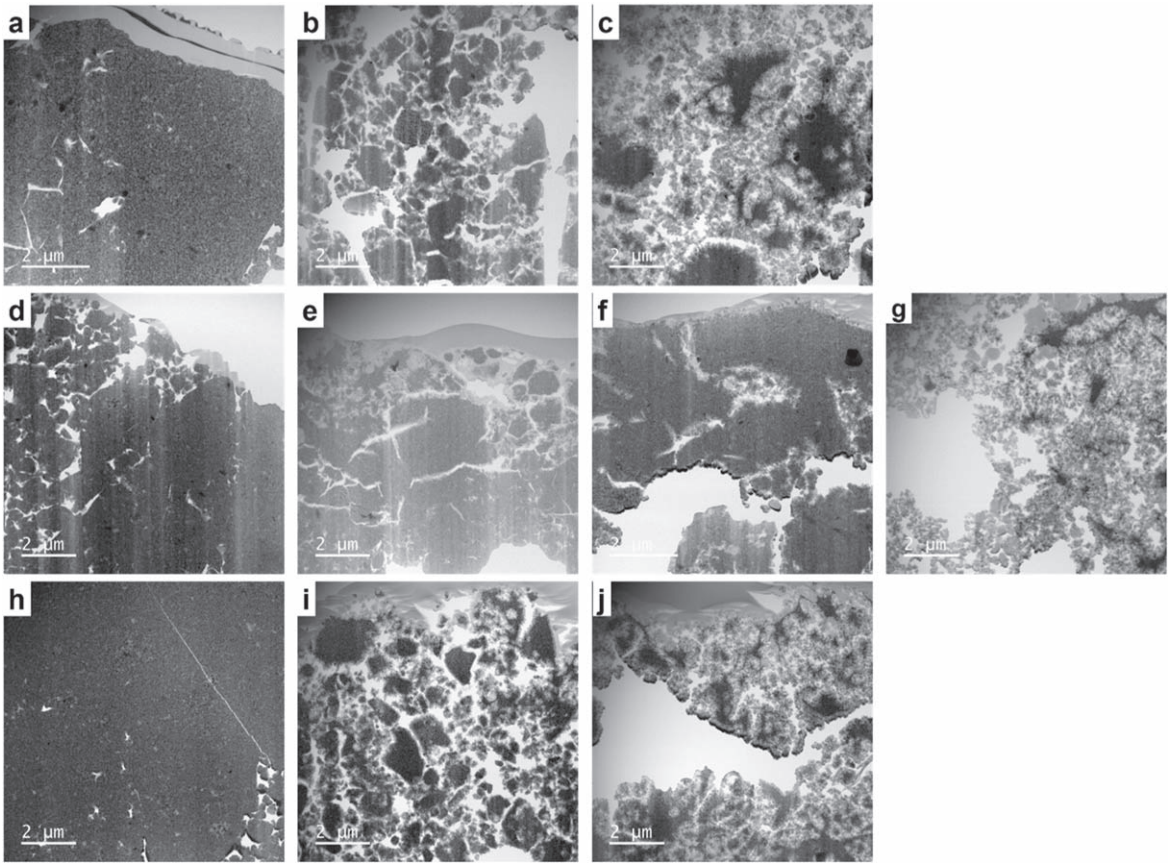

Figure 13. Low-magnification BF-TEM images of (a–c) $LaSi_2/WSi_2/Si$, (d–g) $LaSi_2/CrSi_2/Si$, and (h–j) $LaSi_2/MoSi_2/Si$ electrodes (a, d, and h) before cycling and after the (b, e, and i) 600th, (c, f, and j) 1200th and (g) 1700th cycles. (d)–(g) were identical to Figs. S10a–S10d, respectively.

Conclusions

To further improve the charge–discharge cycle life of $LaSi_2/Si$ nanocomposite anodes for LIBs, we added stiff $CrSi_2$ to $LaSi_2/Si$. The cycle life of the $LaSi_2/CrSi_2/Si$ electrode was longer than those of the $CrSi_2/Si$ and $LaSi_2/Si$ electrodes. Although the microstructural inversion of the $LaSi_2/Si$ electrode was observed, the addition of $CrSi_2$ suppressed the change in the metallographic structure after cycling. Stiff $CrSi_2$ functioned as a support framework, improving the structural stability of the electrode and preventing changes in the metallographic structure. Consequently, a superior cycle life was achieved owing to the synergistic effect of $LaSi_2$ and $CrSi_2$; the former exhibited elasticity to relax the Si-generated stress, and the latter exhibited stiffness to withstand the Si-generated stress and maintain the metallographic structure. We investigated the cycle lives of the prepared $LaSi_2/MSi_2$ (where M = Mo, Nb, Ta, Ti, or W)/Si nanocomposite electrodes. The cycle life improved as the Vickers hardness of M decreased, and the longest cycle life (a reversible capacity of 1000 mA h $g(Si)^{-1}$ for 1800 cycles) was obtained using $NbSi_2$ as the stiff silicide. Although the $LaSi_2/CrSi_2/Si$, $LaSi_2/TaSi_2/Si$, $LaSi_2/TiSi_2/Si$, and $LaSi_2/NbSi_2/Si$ electrodes exhibited the synergistic effect of elastic $LaSi_2$ and stiff MSi_2, no clear synergistic effect was observed when other stiff silicides (M = Mo and W) were used. The trend was observed when $LaSi_2$ was used as the elastic silicide, and it is unclear whether the same trend might not have been obtained in combination with other elastic silicides. Based on the dQ/dV plots, the a-Li-rich phase formed on the $LaSi_2/WSi_2/Si$ and $TaSi_2/LaSi_2/Si$ electrodes, with relatively poor cycle lives, was more than that on the $LaSi_2/MoSi_2/Si$ and $LaSi_2/NbSi_2/Si$ electrodes, with relatively superior performance. Consequently, the latter two electrodes exhibited longer cycle livesowing to suppressed Si expansion and electrode collapse. Other mechanical properties, e.g., fatigue life and fracture toughness, may have influenced electrode collapse. This study provides insights into the synergistic effects of various silicide functions on the charge–discharge cycle life of batteries.

Acknowledgments

TEM was performed at NIMS Battery Research Platform. The authors thank Dr Y. Kimura of the Daido Steel Co. Ltd. for his support in measuring the Vickers hardness ($TiSi_2$). Moreover, the authors thank Ms. N. Hino, Mr T. Yamaga, and R. Tanaka of the Tottori University for their assistance with image analysis. The manuscript was written with contributions from all authors. This study was partially supported by the Japan Society for the Promotion of Science (JSPS) KAKENHI (Grant numbers JP24K08565, JP20H00399, and JP23K26758) and NIMS Joint Research Hub Program.

ORCID

Yasuhiro Domi https://orcid.org/0000-0003-3983-2202
Hiroyuki Usui https://orcid.org/0000-0002-1156-0340
Kei Nishikawa https://orcid.org/0000-0002-7718-7606
Hiroki Sakaguchi https://orcid.org/0000-0002-4125-7182

References

1. J. M. Tarascon and M. Armand, "Issues and challenges facing rechargeable lithium batteries." *Nature*, **414**, 359 (2001).
2. M. Armand and J. M. Tarascon, "Building better batteries." *Nature*, **451**, 652 (2008).
3. M. S. Whittingham, "Lithium batteries and cathode materials." *Chem. Rev.*, **104**, 4271 (2004).
4. J. B. Goodenough and Y. Kim, "Challenges for rechargeable Li batteries." *Chem. Mater.*, **22**, 587 (2010).
5. M. N. Obrovac and L. J. Krause, "Reversible cycling of crystalline silicon powder." *J. Electrochem. Soc.*, **154**, A103 (2007).

6. B. Key, M. Morcrette, J. M. Tarascon, and C. P. Grey, "Pair distribution function analysis and solid state NMR studies of silicon electrodes for lithium ion batteries: understanding the (De)Lithiation." *Mechanisms. J. Am. Chem. Soc.*, **133**, 503 (2011).
7. S. C. S. Lai, "Lithium-silicon electrode." *J. Electrochem. Soc.*, **123**, 1196 (1976).
8. M. N. Obrovac and L. Christensen, "Structural changes in silicon anodes during lithium insertion/extraction." *Electrochem. Solid-State Lett.*, **7**, A93 (2004).
9. X. H. Liu, L. Zhong, S. Huang, S. X. Mao, T. Zhu, and J. Y. Huang, "Size-dependent fracture of silicon nanoparticles during lithiation." *ACS Nano*, **6**, 1522 (2012).
10. Y. Domi, H. Usui, K. Yamaguchi, S. Yodoya, and H. Sakaguchi, "Silicon-based anodes with long cycle life for lithium-ion batteries achieved by significant suppression of their volume expansion in ionic-liquid electrolyte." *ACS Appl. Mater. Interfaces*, **11**, 2950 (2019).
11. N. Ding, J. Xu, Y.-X. Yao, G. Wegner, X. Fang, C. H. Chen, and I. Lieberwirth, "Determination of the diffusion coefficient of lithium ions in Nano-Si." *Solid-State Ionics*, **180**, 222 (2009).
12. J. Xie, N. Imanishi, T. Zhang, A. Hirano, Y. Takeda, and O. Yamamoto, "Li-Ion diffusion in amorphous Si films prepared by RF magnetron sputtering: a comparison of using liquid and polymer electrolytes." *Mater. Chem. Phys.*, **120**, 421 (2010).
13. Y. Domi, H. Usui, H. Itoh, and H. Sakaguchi, "Electrochemical lithiation and delithiation properties of ceria-coated silicon electrodes." *J. Alloys Compd.*, **695**, 2035 (2017).
14. R. Maddipatla, C. Loka, and K.-S. Kee, "Exploring the potential of carbonized Nano-Si within G@C@Si anodes for lithium-ion rechargeable batteries." *ACS Appl. Mater. Interfaces*, **15**, 58437 (2023).
15. J. Y. Li, G. Li, J. Zhang, Y. X. Yin, F. S. Yue, Q. Xu, and Y. G. Guo, "Rational design of Robust Si/C microspheres for high-tap-density anode materials." *ACS Appl. Mater. Interfaces*, **11**, 4057 (2019).
16. H. Wang, J. Fu, C. Wang, J. Wang, A. Yang, C. Li, Q. Sun, Y. Cui, and H. Li, "A binder-free high silicon content flexible anode for Li-Ion batteries." *Energy Environ. Sci.*, **13**, 848 (2020).
17. M. Je, D.-Y. Han, J. Ryu, and S. Park, "Constructing pure Si anodes for advance lithium batteries." *Acc. Chem. Res.*, **56**, 2213 (2023).
18. H. J. Kwon, J. Y. Hwang, H. J. Shin, M. G. Jeong, K. Y. Chung, Y. K. Sun, and H. G. Jung, "Nano/microstructured silicon–carbon hybrid composite particles fabricated with corn starch biowaste as anode materials for li-ion batteries." *Nano Lett.*, **20**, 625 (2020).
19. E. Mados, N. Harpak, G. Levi, F. Patolsky, E. Peled, and D. Golodnitsky, "Synthesis and electrochemical performance of silicon-nanowire alloy anodes." *RSC Adv.*, **11**, 26586 (2021).
20. X. Zhou, Y. X. Yin, A. M. Cao, L. J. Wan, and Y. G. Guo, "Efficient 3D conducting networks built by graphene sheets and carbon nanoparticles for high-performance silicon anode." *ACS Appl. Mater. Interfaces*, **4**, 2824 (2012).
21. Z. Wang, Z. Xu, Y. Yuan, X. Teng, Z. Pu, Y. Wang, A. Fu, Y.-G. Guo, and H. Li, "Microspheres comprise Si nanoparticles modified with TiO_2 and wrapped by graphene as high-performance anode for lithium-ion batteries." *Appl. Surf. Sci.*, **598**, 153790 (2022).
22. G. Zhu, R. Guo, W. Luo, H. K. Liu, W. Jiang, S. X. Dou, and J. Yang, "Boron doping-induced interconnected assembly approach for mesoporous silicon oxycarbide architecture." *Natl Sci. Rev.*, **8**, nwaa152 (2021).
23. Y. Dong, C. Liu, F. Li, H. Jin, B. Li, F. Ding, Y. Yang, Z. Yang, and F. Yuan, "Highly conductive ultrafine N-Doped silicon powders prepared by high-frequency thermal plasma and their application as anodes for lithium-ion batteries." *ACS Appl. Electron. Mater.*, **6**, 816 (2024).
24. Y. Domi, H. Usui, M. Shimizu, Y. Kakimoto, and H. Sakaguchi, "Effect of phosphorus-doping on electrochemical performance of silicon negative electrodes in lithium-ion batteries." *ACS Appl. Mater. Interfaces*, **8**, 7125 (2016).
25. B. R. Long, M. K. Y. Chan, J. P. Greeley, and A. A. Gewirth, "Dopant modulated Li insertion in Si for battery anodes: theory and experiment." *J. Phys. Chem. C*, **115**, 18916 (2011).
26. S. Yodoya, Y. Domi, H. Usui, and H. Sakaguchi, "Applicability of an ionic liquid electrolyte to a phosphorus-doped silicon negative electrode for lithium-ion batteries." *ChemistrySelect*, **4**, 1375 (2019).
27. Y. Domi, H. Usui, A. Ando, K. Nishikawa, and H. Sakaguchi, "Analysis of the Li distribution in Si-based negative electrodes for lithium-ion batteries by soft X-ray emission spectroscopy." *ACS Appl. Energy Mater.*, **3**, 8619 (2020).
28. Y. Domi, H. Usui, D. Iwanari, and H. Sakaguchi, "Effect of mechanical pre-lithiation on electrochemical performance of silicon negative electrode for lithium-ion batteries." *J. Electrochem. Soc.*, **164**, A1651 (2017).
29. Y. Domi, H. Usui, N. Ieuji, K. Nishikawa, and H. Sakaguchi, "Lithiation/delithiation properties of lithium silicide electrodes in ionic-liquid electrolytes." *ACS Appl. Mater. Interfaces*, **13**, 3816 (2021).
30. M. Saito, K. Kato, S. Ishii, K. Yoshii, M. Shikano, H. Sakaebe, H. Kiuchi, T. Fukunaga, and E. Matsubara, "Effective bulk activation and interphase stabilization of silicon negative electrode by lithium pre-doping for next-generation batteries." *J. Electrochem. Soc.*, **166**, A5174 (2019).
31. H. Sakaguchi, T. Iida, M. Itoh, N. Shibamura, and T. Hirono, "Anode properties of $LaSi_2$/Si composite thick-film electrodes for lithium secondary batteries." *IOP Conf. Ser.: Mater. Sci. Eng.*, **1**, 012030 (2009).
32. H. Usui, K. Meabara, K. Nakai, and H. Sakaguchi, "Anode properties of composite thick-film electrodes consisted of Si and various metal silicides." *Int. J. Electrochem. Sci.*, **6**, 2246 (2011).
33. H. Usui, M. Shimizu, and H. Sakaguchi, "Applicability of ionic liquid electrolytes to $LaSi_2$/Si composite thick-film anodes in lithium-ion battery." *J. Power Sources*, **235**, 29 (2013).
34. H. Usui, K. Nouno, Y. Takemoto, K. Nakada, A. Ishii, and H. Sakaguchi, "Influence of mechanical grinding on lithium insertion and extraction properties of iron silicide/silicon composites." *J. Power Sources*, **268**, 848 (2014).
35. Y. Domi, H. Usui, Y. Takemoto, K. Yamaguchi, and H. Sakaguchi, "Improved electrochemical performance of lanthanum silicide/silicon composite electrode with nickel substitution for lithium-ion batteries." *J. Phys. Chem. C*, **120**, 16333 (2016).
36. Y. Domi, H. Usui, E. Nakabayashi, Y. Kimura, and H. Sakaguchi, "Effect of element substitution on electrochemical performance of silicide/Si composite electrodes for lithium-ion batteries." *ACS Appl. Energy Mater.*, **3**, 7438 (2020).
37. Y. Kimura, Y. Domi, H. Usui, and H. Sakaguchi, "Anode properties of $Cr_xV_{1-x}Si_2$/Si composite electrodes for lithium-ion batteries." *ACS Omega*, **6**, 8862 (2021).
38. Y. Kimura, Y. Domi, H. Usui, and H. Sakaguchi, "Improved cycling performance of $Cr_xV_{1-x}Si_2$/Si composite electrode for application to lithium-ion battery anodes." *J. Electrochem. Soc.*, **169**, 010537 (2022).
39. Y. Domi, H. Usui, K. Nishikawa, and H. Sakaguchi, "Metallographic structure changes in lanthanum silicide/silicon nanocomposite electrodes during lithiation and delithiation: implications for battery applications." *ACS Appl. Nano Mater.*, **4**, 8473 (2021).
40. Y. Kimura, Y. Domi, H. Usui, and H. Sakaguchi, "Lithiation and delithiation properties of silicide/Si composite alloy electrodes prepared by rapid quenching methode." *Electrochemistry*, **88**, 330 (2020).
41. N. Umirov, D. H. Seo, H. Y. Kim, and S. S. Kim, "Grain size effect of nanocrystalline-Si embedded in buffering alloy-matrix as anode for li-ion batteries." *J. Alloys Compd.*, **882**, 160558 (2021).
42. H. Sakaguchi, T. Toda, Y. Nagao, and T. Esaka, "Anode properties of lithium storage alloy electrodes prepared by gas-deposition." *Electrochem. Solid-State Lett.*, **10**, J146 (2007).
43. H. Usui, Y. Kiri, and H. Sakaguchi, "Effect of carrier gas on anode performance of Si thick-film electrodes prepared by gas-deposition method." *Thin Solid Films*, **520**, 7006 (2012).
44. J. A. Akedo, "Deposition of ceramic thick films at room temperature: densification mechanism of ceramic layers." *J. Am. Ceram. Soc.*, **89**, 1834 (2006).
45. J. Akedo, "Room temperature impact consolidation (RTIC) of fine ceramic powder by aerosol deposition method and applications to microdevices." *J. Therm. Spray Tech.*, **17**, 181 (2008).
46. M.-J. Earle, J.-M.-S.-S. Esperança, M.-A. Gilea, J.-N. Lopes, L.-P.-N. Rebelo, J.-W. Magee, K.-R. Seddon, and J.-A. Widegren, "The distillation and volatility of ionic liquids." *Nature*, **439**, 831 (2006).
47. P. Hapiot and C. Lagrost, "Electrochemical reactivity in room-temperature ionic liquids." *Chem. Rev.*, **108**, 2238 (2008).
48. P. Sippel, P. Lunkenheimer, S. Krohns, E. Thoms, and A. Loidl, "Importance of liquid fragility for energy applications of ionic liquids." *Sci Rep.*, **5**, 13922 (2015).
49. A. Ghoufi, A. Szymczyk, and P. Malfreyt, "Ultrafast diffusion of ionic liquids confined in carbon nanotubes." *Sci Rep.*, **6**, 28518 (2016).
50. Y. Domi, H. Usui, A. Ueno, Y. Shindo, H. Mizuguchi, T. Komura, T. Nokami, T. Itoh, and H. Sakaguchi, "Effect of annealing temperature of Ni-P/Si on its lithiation and delithiation properties." *J. Electrochem. Soc.*, **167**, 040512 (2020).
51. Y. Domi, H. Usui, R. Takaishi, and H. Sakaguchi, "Lithiation and delithiation reactions of binary silicide electrodes in an ionic liquid electrolyte as novel anodes for lithium-ion batteries." *ChemElectroChem*, **6**, 581 (2019).
52. Y. Domi, H. Usui, K. Sugimoto, K. Gotoh, K. Nishikawa, and H. Sakaguchi, "Reaction behavior of a silicide electrode with lithium in an ionic-liquid electrolyte." *ACS Omega*, **5**, 22631 (2020).
53. Y. Domi, H. Usui, T. Ando, and H. Sakaguchi, "Impact of the crystalline phase of binary silicide on its lithiation and delithiation properties." *Mater. Adv.*, **3**, 6231 (2022).
54. Y. Domi, H. Usui, Y. Shindo, S. Yodoya, H. Sato, K. Nishikawa, and H. Sakaguchi, "Electrochemical lithiation and delithiation properties of $FeSi_2$/Si composite electrodes in ionic-liquid electrolyte." *Electrochemistry*, **88**, 548 (2020).
55. D. Liu, Y. Huang, L. Liu, and L. Zhang, "A novel of MSi_2 high-entropy silicide: be expected to improved mechanical properties of $MoSi_2$." *Mater. Lett.*, **268**, 127629 (2020).